JOURNAL OF PROPULSION AND POWER
Vol. 18, No. 1, January–February 2002

Cascade Arc Studies of Hydrogen/Nitrogen Plasmas in Nonequilibrium

Trevor Moeller,* Dennis Keefer,† and Robert Rhodes‡
University of Tennessee Space Institute, Tullahoma, Tennessee 37388

A cascade arc facility was developed to study the characteristics of nonequilibrium plasma propellants for electric propulsion applications. The cascade arc was operated with 50 A hydrogen arcs at absolute pressures of 1.34×10^4 and 4.14×10^4 Pa. Spatially resolved spectral emission data were collected using a two-dimensional optical multichannel analyzer (OMA), and radial distributions of H_α line widths of the Abel inverted emission line profiles were obtained. The measured H_α line widths were compared to values predicted by nonequilibrium cascade arc simulations using the UTSI Cascade Arc Plasma Simulation (CAPS) code and dynamic ion Stark broadening/electron number density correlations. Agreement was sensitive to the finite-rate kinetic model used for hydrogen. When used in CAPS, University of Illinois kinetics model gave the best agreement with the hydrogen cascade arc measurements. The experimental electric field and radially resolved H_α line widths accurately predicted measured values at both pressures within experimental uncertainty. H_α line widths for simulated ammonia and hydrazine were also obtained at pressures of 1.34×10^4, 4.14×10^4, and 6.89×10^4 Pa. These mixture data can be used for future evaluations of kinetic models for hydrogen/nitrogen mixtures.

Nomenclature

A	=	Arrhenius constant
$\boldsymbol{B}$	=	magnetic field vector
C_p	=	mixture specific heat
c_{pi}	=	molar specific heat at constant pressure
D	=	effective mixture diffusion coefficient
E	=	activation energy
e	=	electron
H	=	static enthalpy of gas
H	=	hydrogen
H_2	=	diatomic hydrogen
H^+	=	hydrogen ion
h_i	=	molar enthalpy of specie i
$\boldsymbol{J}$	=	current density vector
K_p	=	equilibrium constant
k	=	thermal conductivity
k_b	=	backward kinetic reaction-rate coefficients
k_f	=	forward reaction-rate coefficient
k_R	=	Rosseland thermal conductivity
M	=	mixture molecular weight
p	=	pressure
q_{ce}	=	transfer of energy between the heavy gas and the electron gas resulting from collisions
q_{ch}	=	energy transport to the electron gas caused by electron participation in chemical reactions
q_i	=	ohmic heating, J_x^2/σ
q_r	=	loss caused by optically thin radiation
R	=	universal gas constant
r	=	radius
S	=	source term
S_α	=	production of the species by chemical reaction
T	=	temperature
u	=	axial velocity
$\boldsymbol{v}$	=	gas velocity vector
x	=	mole fraction
α_i	=	concentration of plasma constituent i
Γ	=	represents a transport coefficient
μ	=	viscosity
ρ	=	gas density
σ	=	electrical conductivity
τ	=	viscous stress tensor
υ_i	=	collision frequency
Φ	=	viscous dissipation
φ	=	dummy variable representing the axial velocity

Subscripts

e	=	electron
h	=	heavy particles
i	=	counter referring to species
r	=	radiation
x	=	axial direction

Received 14 October 1998; revision received 14 May 2001; accepted for publication 11 June 2001.

*Research Engineer, InnovaTek, Inc., 350 Hills Street, Richland, WA 99352. Associate Member AIAA.
†B.H. Goethert Professor of ES. Senior Member AIAA.
‡Senior Engineer. Senior Member AIAA.

I. Introduction

ELECTRIC propulsion thrusters offer significant improvements in performance over conventional thrusters utilized for satellite station keeping and maneuvering. Computational codes can be used to guide refinements in the configuration of electric propulsion thrusters that lead to improved thruster performance. Several computer simulation codes have been developed for this purpose.[1–4] However, it is clear that important nonequilibrium processes in the propellant plasma must be understood before accurate physical models can be constructed for use in these computational codes. The University of Tennessee Space Institute (UTSI) cascade arc facility allows accurate diagnostic measurements of nonequilibrium propellant plasma properties. These measurements have been used to evaluate the kinetic models and transport properties utilized in electric propulsion thruster computational codes.

II. Use of the Cascade Arc for Nonequilibrium Plasma Research

Cascade arcs have long been used as a means to measure the fundamental atomic constants and transport properties of high-temperature gases.[5] The cascade arc has a flow velocity much smaller than seen in electric propulsion thrusters, and the length of the arc plasma in the cascade is tens of diameters compared to one diameter that is typical in electric propulsion devices. This produces

cascade arc plasmas with properties similar to propellant plasmas in electric propulsion thrusters but with negligible axial gradients. Therefore, a balance between radial diffusion and chemical reactions with an axially constant, but radially dependent energy input determines the nonequilibrium plasma state in a cascade arc. As a result, plasma properties depend on the local conditions at the measurement station rather than a complex space-time convolution of all of the conditions upstream of the point of measurement (as is realized in a thruster). Thus, differences between code predictions and measured quantities are more easily related to the specific reactions or diffusion rates used by the code.

III. UTSI Cascade Arc Facility

The UTSI cascade arc is comprised of individually water-cooled copper plates separated by electrical insulators (see Fig. 1). These plates are 3.18 mm thick and form a 4-mm-diam arc channel that is approximately 40 mm long when stacked together. The insulators are binderless ceramic paper (alumina and silica) 0.25 mm thick. O-rings are positioned between the plates to prevent air from contaminating the test gas in the arc channel. Optical access is allowed through a modified water-cooled copper plate with windows. This section is located in the center of the cascade arc to minimize end effects. The arc is driven by a 50 A, 600 V D.C. power supply. A cascaded centrifugal pump delivers cooling water to the copper plates and electrodes to allow continuous operation of the arc.

Spectrally resolved emission data from the propellant plasma are collected using the optical setup shown in Fig. 2. To eliminate arc asymmetries caused by buoyancy, the cascade arc is positioned vertically. An adjustable Cassegrain telescope is used to provide a small-entrance solid angle for the cascade window section and to avoid off-axis aberrations.[6] This collects light from the arc and directs it into a 1.25-m focal-length spectrometer so that the primary mirror in the spectrometer is overfilled. The light from the arc is rotated 90 deg before entering the telescope so that the radial dimension of the arc image lies along the slit. Spatially resolved spectral data are collected and digitized using a two-dimensional optical multichannel analyzer (OMA) with an image intensifier. This detector has a 512×512 pixel detector array with 19-μm pixel spacing. The magnification of the optical system is approximately 1.0, providing 200 pixel resolution across the 4-mm-diam arc channel. Further details of the experimental setup may be found in Ref. 6.

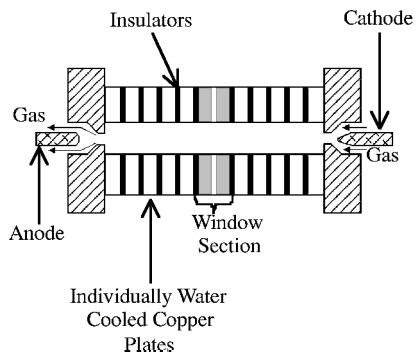

Fig. 1 Cascade arc assembly.

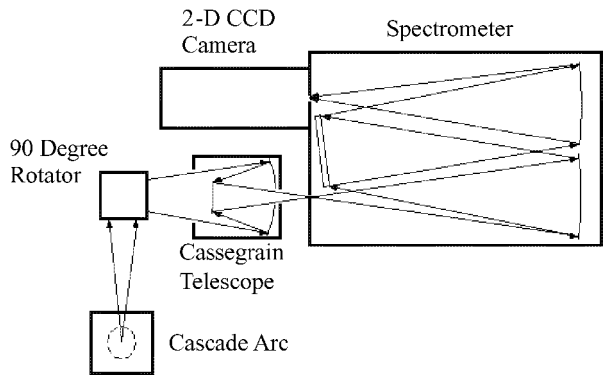

Fig. 2 Schematic of the optical setup.

IV. UTSI Cascade Arc Plasma Simulation (CAPS) Code

The two-dimensional equilibrium and nonequilibrium UTSI arcjet computer codes[7] have been modified into pseudo-one-dimensional nonequilibrium and equilibrium cascade arc plasma simulation (CAPS) codes. The nonequilibrium version includes species diffusion, finite-rate chemical kinetics for H_2, H, H^+ and electrons, and uses a two-temperature model with separate energy equations for electrons and heavy species. These viscous Navier–Stokes codes also include radiation transport, where the optically thin portion of the spectrum is assumed to be directly lost from the system, and the optically thick resonance radiation is modeled using the Rosseland approximation to form an enhanced thermal conductivity.[8]

Because of symmetry and small axial flow velocities in the arc, the following assumptions are made: 1) the radial pressure gradient is zero, 2) the radial and azimuthal velocities are zero, 3) the radial current density is zero, and 4) the axial species gradients are zero. Early cascade arc models included axial species gradients. These gradients where found to be neglible but negatively impact CAPS code convergence. Therefore these terms were eliminated from the current study. The axial velocity is calculated, but the small velocities lead to insignificant axial gradients that have little effect on the simulations.[8] The required mass flow is ensured by adjustment of the velocity. A no-slip condition consistent with a viscous flow model is forced by specifying a zero axial velocity at the wall. The wall has a specified temperature and is assumed to be catalytic for electron-ion recombination and hydrogen-atom recombination. This leads to an equilibrium condition at the wall with the gas enthalpy specified by the pressure and the wall temperature. The catalytic wall condition is specified for both the nonequilibrium and the equilibrium codes.[7] The consequence of these assumptions is that species production and diffusion are locally balanced and total production is balanced by wall losses for the axial momentum, energy, electron energy, and species concentration.[7]

Numeric Model and Governing Equations

The algorithm for the CAPS code is a Navier–Stokes solver based on the SIMPLE (Semi-Implicit Pressure Linked Equation) algorithm developed by Gosman and Pun[9] and modified by Rhie[10] to accommodate both supersonic and subsonic flow.[11] Jeng[12] and Keefer and Rhodes and Keefer[13] incorporated a magnetic field equation coupled with heat release to study laser heat addition and radio frequency heating of a plasma, respectively. The code is formulated to solve the steady-state Navier–Stokes equations. The governing equations in the code are solved in a transformed coordinate where the original, nonorthogonal, axially symmetric grid is mapped to a grid of unit squares.[14] Assumptions in the code specify the radial velocity and radial current density to be zero. The radial pressure gradient is also specified to be zero. The axial velocity and pressure are, however, allowed to vary axially.

The SIMPLE algorithm used in the CAPS code is a solver for equations of the form

$$\nabla \cdot \rho v \varphi = \nabla \cdot \Gamma_\varphi \nabla \varphi + S \tag{1}$$

Any terms that cannot be put into a convective or diffusive form are added to the source term S[7]. Second-order-accurate finite difference representations are used to represent Eq. (1) for the variable under consideration at each point in the computation grid. Written in matrix form, these coupled equations result in a tridiagonal matrix that is solved using a tridiagonal solver. Equation (1) is solved sequentially for each of the dependent variables using underrelaxation. Updated values of the dependent variables are used when they are available, and old values are used when the variables have not yet been updated. The process of solving Eq. (1) for each of the dependent variables is repeated until the sum of all of the residual errors has been reduced to a small value.[7] At this point the numerical solution to the problem is no longer changing significantly.

Momentum Equation

The form of the momentum conservation equation is the same for both the equilibrium and nonequilibrium cases. The axial velocities are obtained from the axial momentum equation for steady, axially symmetric flow.[14] The momentum equation, in vector form, is[2]

$$\nabla \cdot \rho \boldsymbol{v} \cdot \boldsymbol{v} = -\nabla p + \nabla \cdot \tau + \boldsymbol{J} \times \boldsymbol{B} \tag{2}$$

Because the current only has an axial component and the magnetic field only has an azimuthal component, the Lorentz force, the cross product of $\boldsymbol{J}$ and $\boldsymbol{B}$, is in the radial direction. The flow in the cascade is assumed to be axial; therefore, the Lorentz force in the radial direction has no effect on the momentum equation.

The densities for the equilibrium and nonequilibrium versions of the CAPS code are given by Eqs. (3) and (4), respectively[7]:

$$\rho = \frac{pM}{RT} \tag{3}$$

$$\rho = \frac{pM}{R[T_h - (T_e - T_h)x_e]} \tag{4}$$

The addition of the mass continuity equation $\nabla \cdot (\rho u) = 0$ allows the pressure to be calculated.[2] Because the mass flow rate in the cascade arc is very small, the axial velocities realized in the constrictor channel are also very small (approximately 10 m/s). These low velocities result in axial pressure gradients that do not significantly affect simulation results.

Equilibrium Energy Equation

The equilibrium CAPS code assumes local thermodynamic equilibrium (LTE). This assumption implies that the temperature of all of the particles in the gas is the same, and only one energy equation is necessary to describe a plasma. The static enthalpy H is obtained from the following energy equation that includes ohmic heating, radiation loss, and viscous dissipation.[2]

$$\nabla \cdot \rho \boldsymbol{v} H = \nabla \cdot (k/C_p)\nabla H + \Phi + q_i - q_r + \boldsymbol{v} \cdot \nabla p \tag{5}$$

where the viscous dissipation is

$$\Phi = \mu \left[2\left(\frac{\partial u}{\partial x}\right)^2 + \left(\frac{\partial u}{\partial r}\right)^2 - \frac{2}{3}\left(\frac{\partial u}{\partial x}\right)^2 \right] \tag{6}$$

Nonequilibrium Energy Equation

Because the LTE assumption is relaxed in the nonequilibrium CAPS code, the temperature of the electrons is not necessarily equal to the temperature of the heavy particles. Therefore, the energy in the system must be represented by two energy equations. The equation for the mixture enthalpy H is[7]

$$\nabla \cdot \rho \boldsymbol{v} H = \nabla \cdot \left[\frac{k}{C_{p_h}} \nabla H + \left(\rho D - \frac{k}{C_{p_h}} \right) \sum h_i \nabla \alpha_i - k \alpha_e \frac{C_{p_e}}{C_{p_h}} \nabla T_e \right] + \Phi + q_i - q_r + \boldsymbol{v} \cdot \nabla p \tag{7}$$

An equation representing the energy in the electron gas is the other equation chosen to represent the energy in the two-temperature system. In this equation the electrical ohmic heating is balanced by electron conduction, convection, diffusion, and energy transport to the heavy particles through collisions.[7] The form of the equation is[15]

$$\nabla \cdot \rho \boldsymbol{v} \alpha_e h_e - \nabla \cdot (k_e \nabla T_e + h_e D \nabla \alpha_e) - \boldsymbol{v} \cdot \nabla p_e = S \tag{8}$$

where the source term $S = q_{ce} + q_{ch} + q_i - q_r$. The last term on the left-hand side of Eq. (8) describes the work done by the electron-pressure gradients. This term is determined using the assumption that the velocities of the heavy species and electrons are the same in the flow. The partial pressure of the electrons is given by[7]

$$p_e = \frac{pT_e x_e}{T_h + (T_e - T_h)x_e} \tag{9}$$

"The term q_{ce} represents the transfer of energy between the heavy gas and the electron gas resulting from collisions of electrons with heavy species,"[7]

$$q_{ce} = \sum_i^{h.p.} 2n_e \frac{m_e}{m_i} \upsilon_i \frac{3}{2} k(T - T_e) \tag{10}$$

where υ_i is the collision frequency and the summation is over the species in the heavy gas. "The collision frequency is evaluated from the temperature dependent collision cross-sections for electron-heavy collisions evaluated at the electron temperature using the transport property [routines] described below."[7]

Energy transport to the electron gas caused by electron participation in chemical reactions is represented by the term q_{ch} in Eq. (8). The energy released by a three-body recombination reaction with the electron acting as the third body is assumed to be absorbed into the electron gas, raising the electron temperature. Ionization and dissociation caused by electron collision is assumed to remove the dissociation or ionization energy from the electron gas, lowering the electron temperature.[7]

The electrical energy input to the system q_i is the same ohmic heating used in the equilibrium simulation. The optically thin radiation q_r is the same for both the equilibrium and nonequilibrium simulations.

Species

Because the equilibrium CAPS code assumes LTE and chemical equilibrium, species concentrations are a function of pressure and temperature, which are defined by the Saha equation.[16] For the nonequilibrium CAPS code finite-rate chemical kinetics must be included in the CAPS code model.

The system of governing equations utilized in the nonequilibrium CAPS code are expanded to include three species equations. This allows the calculation of systems where ionization of H and the dissociation of H_2 are not in equilibrium.[7] The hydrogen system is modeled as a four-component system: molecular hydrogen, H_2; atomic hydrogen, H; hydrogen ions, H^+; and electrons, e. Because the system is electrically neutral, the electrons and hydrogen ions can be represented by the same species conservation equation (this allows the four-species system to be modeled by three species concentration equations). The species conservation equation used in the CAPS code is[7]

$$\nabla \cdot \rho \boldsymbol{v} \alpha = \nabla \cdot \rho D \nabla \alpha + S_\alpha \tag{11}$$

Because the species are assumed to vary only radially and the radial velocity is zero, the term on the left side of Eq. (8) is zero. Because of constraints in the SIMPLE algorithm, the source term S_α must be evaluated before the species equations can be solved. If each computation cell is assumed to be a well-stirred reactor, the time available for chemical reactions to occur would be the characteristic time for a well-stirred reactor. This characteristic time is calculated from the mass in the computation cell of interest divided by the mass flux into the cell.[7] The nonlinear nature of the chemical rate equations, however, requires that the species production be evaluated using a much smaller time step—the chemical time step—that is a fraction of the characteristic time for a well-stirred reactor. The species conservation equations are then solved over this smaller time step using a linearized set of equations for the four hydrogen species.[17] The source term for each cell is equal to the change in species concentration divided by the chemical time step.

The species production needed in the preceding calculation is determined from chemical kinetic reaction-rate coefficients. The forward reaction-rate coefficients are calculated from the Arrhenius equation[18]

$$k_f = AT^{-n} \exp(E/RT) \tag{12}$$

The Arrhenius constant, the activation energy, and the power of the temperature n are user input to the CAPS program. The backward kinetic reaction-rate coefficients k_b are calculated from k_f and the equilibrium constant K_p.[18]

$$k_b = -k_f / K_p \tag{13}$$

The calculated reaction rates can vary greatly for a chemical reaction depending upon the kinetic rate constants used in Eq. (12). The species concentrations obtained from the computer simulations are extremely sensitive to the calculated rate constants.

Furthermore, a significant amount of the energy is transported between the electrons and the heavy species when an electron acts as the third body in a reactive collision.[6] As a result, the recombination reaction rates can influence the electron to heavy gas temperature ratio, as well as the gas composition.

Transport Properties

The transport properties for both the equilibrium and nonequilibrium versions of the CAPS code are calculated using a computer code written by Cho[19] based on the procedures developed by DeVoto.[20] The transport property models used in this reference are based on the Chapman–Enskog method.[21,22] The models in Cho's code start with experimental or calculated energy-dependent collision cross sections, calculate the collision integrals based on one of several interaction models, and use combinations of the collision integrals to determine the transport properties. Electrical conductivity and electron thermal conductivity depend on collisions between electrons and heavy species in the mixture, whereas viscosity and heavy gas thermal conductivity depend primarily on collisions between the heavy species.[6]

The Cho model makes the following assumptions when used with a two-temperature nonequilibrium plasma model. The fundamental cross-section data describe the interaction of one atom or molecule with another and depends only upon collision energy and the identity of the colliding pair. The nonequilibrium plasma is described by a two-temperature model where a Maxwellian distribution at a unique electron temperature describes the kinetic energy of the electrons. The electron temperature is used to determine the collision energy for all collisions involving electrons because the relative velocity of a collision involving an electron is close to the velocity of the electron. The heavy gas temperature is used to determine the collision energy for all other collisions.[6]

Species diffusion in the CAPS code utilizes the binary diffusion coefficients. Ambipolar diffusion coefficients are used where positively charged particles (H^+) and negatively charged particles (e) diffuse. In the plasma flows seen in a cascade arc, it is assumed that there are very few locations where H_2 and the ion/electron pair coexist. Therefore, a single effective diffusion coefficient is used in the CAPS code for all species rather than the correct, but much more complicated, multicomponent diffusion coefficients.[7] To formulate the species conservation equations in a manner that can be solved by SIMPLE, Rhodes and Keefer[7] created a heuristic mixture rule to provide an effective diffusion coefficient that allows a smooth transition across regions where all four components (H_2, H, H^+, e) coexist.

$$D = \frac{\alpha_{H_2}\alpha_H D_{H_2H} + (\alpha_{H_2}\alpha_{H^+} + \alpha_{H_2}\alpha_e) D_{H_2H^+} + (\alpha_H\alpha_{H^+} + \alpha_H\alpha_e) D_{HH^+}}{\alpha_{H_2}\alpha_H + \alpha_{H_2}\alpha_{H^+} + \alpha_{H_2}\alpha_e + \alpha_H\alpha_{H^+} + \alpha_H\alpha_e} \tag{14}$$

The diffusion coefficients for the H^+/H_2 pair and the H^+/H pair in Eq. (14) are ambipolar diffusion coefficients. Ambipolar diffusion causes the electrons to diffuse into H_2 and H at the same rate as the ions. Therefore, separate binary diffusion coefficients involving electrons are not required. Equation (14) gives the correct answer for any two-component mixture and provides a smooth transition where the mixture has three components.[7] The effective diffusion coefficient is used in the nonequilibrium energy equations [Eqs. (7) and (8)] and the conservation of species equation [Eq. (11)].

Radiation transport is calculated using the methods described by Griem,[16] which include both line and continuum emission. Energy transport through radiation is modeled as having an optically thin part and an optically thick part. The optically thick component is modeled as a thermal conductivity using the Rosseland approximation.[23] The Rosseland thermal conductivity k_R is

$$k_R = (16/3a_R)\sigma T^3 \tag{15}$$

Table 1 Reaction rates for hydrogen [The forward reaction rates given by $k_f = a/T^n \exp(E/RT)$]

Rate set	Reaction	a	n	E
#1, #2, #3[a,b]	$H + H + M \leftrightarrow H_2 + M$	6.40e+17	1.0	0
#1, #2, #3[a,b]	$H^+ + e + M \leftrightarrow H + M$	5.26e+26	2.5	0
#2[c]	$H_2 + e \rightarrow H + H + e$	1.91e+11	−1.0	−203
#3[c]	$H_2 + e \rightarrow H + H + e$	1.87e−3	−3.73	0
#1, #2, #3[c]	$H^+ + e \rightarrow H + h\nu$	3.77e+13	0.58	0
#2, #3[c]	$H^+ + e + e \leftrightarrow H + e$	7.08e+39	4.5	0
#1 recombination[c]	$H^+ + e + e \rightarrow H + e$	2.19e+41	5.06	0
#1 ionization[c]	$H + e \rightarrow H^+ + e + e$	1.81e+14	0	−244,750

[a]M is any third body. [b]Reaction uses heavy particle temperature.
[c]Reaction uses electron temperature.

This Rosseland thermal conductivity is fitted as a function of mixture enthalpy, electron concentration, and pressure for a hydrogen plasma in equilibrium. The resulting equation is used in the nonequilibrium code.[7] Any error associated with this assumption is assumed to be small because optically thick radiation is very small when compared to the other energy transport mechanisms in hydrogen plasmas at pressures and temperatures realized in the UTSI cascade arc. The Rosseland thermal conductivity is added to the internal thermal conductivity of the heavy species to form an effective thermal conductivity for use in the CAPS code simulations when thermal equilibrium is assumed. Otherwise, the Rosseland component is added to the electron thermal conductivity to form an effective electron thermal conductivity.

CAPS code simulations of hydrogen arcs were run for three sets of chemical kinetics that have been utilized in arcjet simulation codes. The reaction rates in these computer simulations are shown in Table 1. Rate set #1 and rate set #2 (Ref. 2) (UTSI arcjet code) have different chemical kinetic rates for the three-body ionization and recombination of hydrogen atoms by electrons. Rate set #3 (Ref. 1) (utilized at the University of Illinois) is the same as rate set #2 but has a different rate for the dissociation of molecular hydrogen by electrons.[24]

V. Experimental Procedure and Data Reduction

The cascade arc was operated at a current of 50 A with pure hydrogen at 1.34×10^4 and 4.14×10^4 Pa. Spectral emission data from the 656.28 nm Balmer alpha H_α line were collected in the eighth order using a 1.25-m Spex spectrometer with a 316 groove/mm Echelle grating and a two-dimensional OMA detector.[6] Nine images of the arc were collected at each pressure. A 1.9 neutral density (ND) filter and a 550-nm high-pass filter were utilized to prevent detector saturation and eliminate interference from higher order lines, respectively. The OMA detector exposure times were 0.2 s for the 4.14×10^4-Pa case and 2.0 s for the 1.34×10^4-Pa case. The images of the arc have 512 spectral pixels and 400 spatial pixels. Wavelength calibration was performed on the spectral pixels using atomic lines from a low-density neon calibration source. The spatial pixels were calibrated by taking images of a 50-μm vertical slit backlit by the neon lamp and placed in the same position as the arc when the cascade is in operation. By moving the vertical slit across the location of the arc with a precision translation table, the spatial pixels were associated with a radial position across the arc region. The spectrometer slit function was experimentally measured using a narrow neon spectral line, and the measured spectral lines were spectrally deconvolved using a digital Wiener filter.[25]

It is well-known that the Stark effect has strong dependence on electron number densities and depends only slightly on temperature. Therefore, the electron number density of a plasma can be determined independently of the plasma temperature by comparing theoretical line widths to the widths of experimentally measured H_α lines.[16] At the pressures tested both Doppler and Stark effects can broaden the experimental emission lines. The resulting line profile is a Voigt profile—a convolution of Gaussian (Doppler) and Lorentzian (Stark) line shapes. For example, a sample Voigt profile fitted to an H_α emission line measured in these experiments is shown in Fig. 3. In this work dynamic ion Stark broadening theory, which

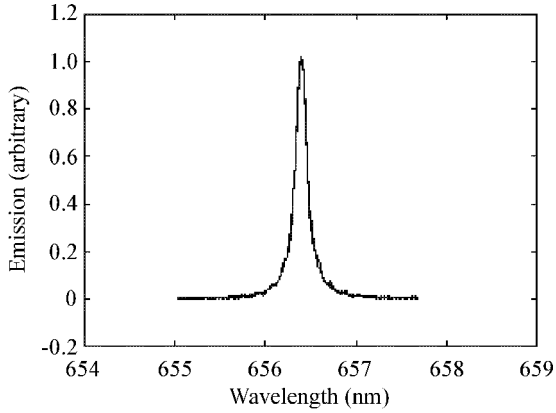

Fig. 3 Measured and fitted theoretical Voigt line shapes of H_α line in a 50-amp hydrogen arc at 4.14×10^4 Pa at a radius of 1.5 mm.

includes the effects of ion motion on the emitting atoms, was used to associate the electron number densities with the broadened emission lines.[26–29] (Results using static ion Stark broadening theory have previously been presented.[6,30,31])

The two-dimensional OMA captures spectral intensity data at many spatial locations across the arc simultaneously. These intensity data are Abel-inverted to obtain radial profiles of the spectral emission using a modern approach that utilizes integral transforms.[32] The uncertainty associated with this Abel-inversion technique is calculated using a method developed by Smith.[33]

After Abel inversion a radial distribution of the H_α emission lines can be compared with those predicted by the CAPS code simulations. The half-widths of each of these lines are easily determined by subtracting the baseline from the line peak and calculating the half-width at half-maximum. This results in a radial distribution of H_α emission line half-widths that can be compared to results from the CAPS code simulations.

At this point line widths predicted using data from the CAPS code simulations are needed for comparison with the measured line widths. Running the CAPS code to a converged solution generates radial distributions of species concentrations, heavy particle temperatures, and electron temperatures. The predicted heavy particle temperatures and electron number densities obtained from the computer simulation can be utilized to calculate the Doppler and Stark-broadened widths of the H_α emission lines. Adding these line widths in quadrature gives the equivalent line width of the Voigt profiles that result from the convolution of the Doppler and Stark line profiles. This results in a radial distribution of Voigt line widths predicted using the CAPS code that can be directly compared to the Abel-inverted line profiles obtained from the experiment.

The spectral measurements just described were repeated for simulated ammonia and simulated hydrazine at pressures of 1.34×10^4, 4.14×10^4, and 6.89×10^4 Pa. Detector exposure times of 2, 5, and 10 s were used for these measurements, respectively.

VI. Comparison of Experimental and Numerical Results for Hydrogen

Comparisons of the radial distributions of calculated and measured H_α emission lines for the 1.34×10^4 Pa (2.0 psi) and 4.14×10^4 Pa (6.0 psi) cases are presented in Figs. 4 and 5, respectively. The centerline line widths correspond to 2.6×10^{21} m^{-3} and 1.3×10^{22} m^{-3} for the 1.34×10^4 and 4.14×10^4 Pa cases, respectively, when dynamic ion Stark broadening theory[26,28] is applied. The computer simulations used the three sets of finite chemical kinetic rates given in Table 1. For the sake of clarity, error bars are not included in Figs. 4 and 5. (Error associated with experiments and computer simulations will be discussed in Sec. VIII.) The line widths are highly influenced by electron number density (Stark broadening) and only slightly influenced by the heavy particle temperature (Doppler broadening) in the pressure ranges considered. Therefore, the profiles of the line width distributions in Figs. 4 and 5 are es-

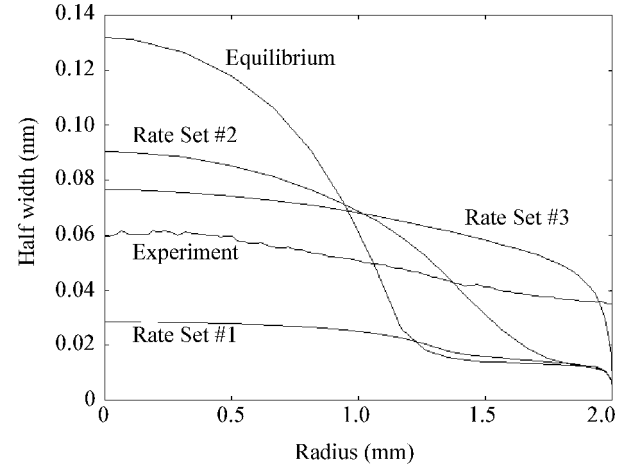

Fig. 4 Comparison of experimental and numerical radial distributions of H_α line widths in a 50-amp hydrogen arc at 1.34×10^4 Pa using chemical kinetic rate sets #1, #2, and #3 in the CAPS code.

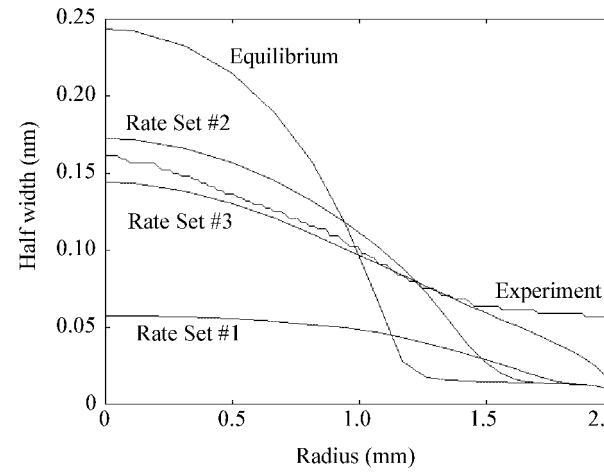

Fig. 5 Comparison of experimental and numerical radial distributions of H_α line widths in a 50-amp hydrogen arc at 4.14×10^4 Pa using chemical kinetic rate set #1, #2, and #3 in the CAPS code.

sentially the same as those for radial profiles of electron number density (this was confirmed with CAPS code data).

The equilibrium computer simulations predict that the electron density becomes negligible beyond a radius of 1.5 mm (Figs. 4 and 5); therefore, the half width half maximum (HWHM) drops off drastically. On the other hand, the nonequilibrium simulations predict significant densities all the way to the wall and have significantly flatter distribution of line widths. This characteristic is also seen in the data, supporting the nonequilibrium nature of the cascade arc plasmas.

At 4.14×10^4 Pa the measured H_α emission widths are bounded by those predicted by the nonequilibrium computer simulations up to a radius of 1.5 mm. At 1.34×10^4 Pa the measured line widths are bounded by the three simulated nonequilibrium electron number densities.

Although the line widths are underpredicted by about a factor of three for the rate set #1 at both pressures, the results for rate set #2 significantly reduce this discrepancy. For small radii the rate set #2 case nearly matches the experiment at 4.14×10^4 Pa and overpredicts the experiment by about 50% at 1.34×10^4 Pa. However, beyond a radius of approximately 1.2 mm the rate set #2 case results in large underpredictions. The rate set #3 case gives the best nonequilibrium solution results; it underpredicts the 4.14×10^4-Pa experimental values by less than 15% and overpredicts the experimental value at 1.34×10^4 Pa by less than 25%. The shapes of the rate set #3 profiles also predict the shapes of the electron number density profiles better than the solutions using any of the other chemistry rate sets.

Table 2 Comparison of experimentally determined electric field (V/cm) with UTSI CAPS code values

Case	Equilibrium simulation	Rate set #1	Rate set #2	Rate set #3	Experiment
1: 1.34×10^4 Pa (2.0 psi)	46.4	95.7	42.0	33.4	36.0 ± 1.2
2: 4.14×10^4 Pa (6.0 psi)	46.3	64.9	43.9	44.1	44.2 ± 1.2

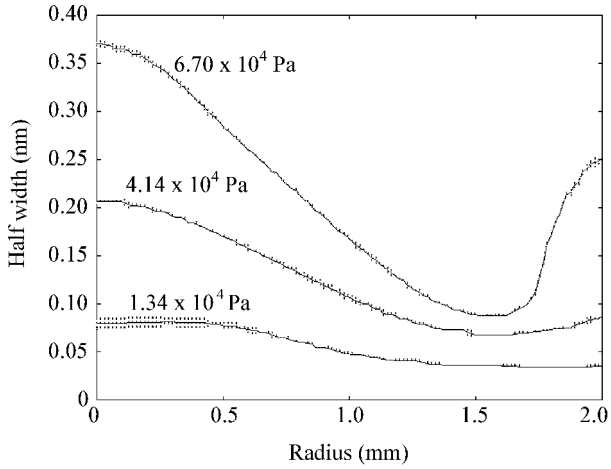

Fig. 6 Radial distributions H_α line widths for simulated ammonia (NH_3) at 1.34×10^4, 4.14×10^4, and 6.70×10^4 Pa.

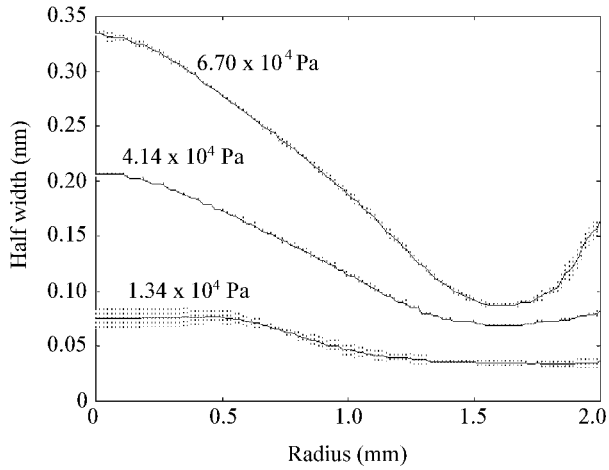

Fig. 7 Radial distributions H_α line widths for simulated hydrazine (N_2H_4) at 1.34×10^4, 4.14×10^4, and 6.70×10^4 Pa.

Table 2 is a comparison of the experimental and CAPS code-predicted axial electric fields for the 1.34×10^4- and 4.14×10^4-Pa cases. The experimental electric fields were determined by finding the slope of the best-fit line through the measured potentials of the cascade plates. The electric fields from the equilibrium simulations overpredict the experimentally determined values by 33% for the 1.34×10^4-Pa case and 10% for the 4.14×10^4-Pa case. These overpredictions increase to 180 and 51% for the rate set #1 simulations at 1.34×10^4 and 4.14×10^4 Pa, respectively. The electric field for the rate set #2 simulations overpredicts the experiment by 17% for 1.34×10^4 Pa and agrees with the value for 4.14×10^4 Pa. The nonequilibrium CAPS simulations using the rate set #3 kinetics best predict the electric field, underpredicting the value for the 1.34×10^4-Pa case by less than 5% and matching the value for the 4.14×10^4-Pa case. It is clear that the chemical kinetic rates exert a strong influence on the predicted axial electric field.

VII. Results for Hydrogen/Nitrogen Mixtures

The radial distribution of experimentally measured H_α emission line half-widths for simulated ammonia and simulated hydrazine are shown in Figs. 6 and 7, respectively. These data show an increase in line width with pressure. An interesting feature of the profiles is the positive slope of the curve close to the wall of the arc channel at 2 mm. This feature is attributed to reflections inside of the cascade channel; some of the light from the broader lines near the arc center is reflected from the optical channel walls so that it appears to be originating closer to the wall of the constrictor. This reflected light effectively broadens the narrower and weaker line emission near the constrictor wall. Low signal level at these larger radii magnifies this effect.[8]

Table 3 Experimentally determined electric field (V/cm) for hydrogen and hydrogen/nitrogen mixtures

Case	Hydrogen	Simulated ammonia	Simulated hydrazine
1: 1.34×10^4 Pa (2.0 psi)	36.0 ± 1.2	26.4 ± 0.7	26.2 ± 0.8
2: 4.14×10^4 Pa (6.0 psi)	44.2 ± 1.2	38.8 ± 1.1	35.1 ± 0.9

Table 3 shows a comparison of experimentally determined electric fields for the hydrogen and hydrogen/nitrogen mixtures. Over the range of pressures tested, the electric field increases with pressure and decreases as more nitrogen is added.

VIII. Discussion of Results

The comparisons between the predicted and measured radial distributions of the H_α emission line widths for the hydrogen arcs show discrepancies ranging from as low as 15% to as high as a factor of two. The magnitude of the discrepancy depends on which chemical kinetic rates were utilized in the CAPS code simulations. The discrepancies result from either error in the CAPS code simulations, experimental error, or a combination of both.

Obviously, incorrect finite-rate chemical kinetics and nonequilibrium transport properties utilized in the CAPS code could be responsible for the discrepancies in the line width distributions. A parametric study was undertaken to determine the effects of artificially changing nonequilibrium transport properties and finite-rate chemical kinetics relative to the rate set #3 chemical kinetic rates.[8] All of the CAPS code solutions were well-converged, and the computation grid was found not to influence the simulation results. Any changes that resulted in a better fit to the measured H_α line widths also created large discrepancies between the predicted and measured axial electric fields, which were originally in good agreement. Therefore, it seems unlikely that changes in the chemical kinetic rates and the nonequilibrium transport properties could resolve the discrepancies in the H_α line widths without adversely affecting the simulated electric field.

To calculate the line broadening predicted using the CAPS code, any uncertainty associated with the dynamic ion Stark-broadened data[26,28] utilized to correlate electron number densities with Stark-broadened line widths introduces error into the line widths predicted by the CAPS code. The authors of the dynamic ion Stark broadening data estimate the error associated with their data to be approximately 20% (Ref. 28). The H_α line widths predicted using the CAPS code that are presented in Figs. 4 and 5 also have 20% error associated with them.

The error in line widths for the CAPS code simulations (with the chemical kinetic rate set #3) resulting from the uncertainty in the Stark broadening correlation is plotted in Figs. 8 and 9 for the 1.34×10^4 Pa (2.0 psi) and 4.14×10^4 Pa (6.0 psi) cases, respectively. The error bars on the measured line widths are plus or minus one standard deviation for the nine realizations obtained at each pressure. The error from Abel inversion is not included because it was found to be significant only at very small radii. It is easily seen in these plots that CAPS code simulation and experimentally measured line widths actually are in agreement over the entire radius of the cascade arc constrictor when uncertainties associated with each are considered. The only discrepancies that still remain are near the wall and can easily be attributed to low signal to noise ratio in this region (to be discussed later).

The error bars on the measured line width data (Figs. 8 and 9) are attributed to the quality of the experimental emission profiles.[8]

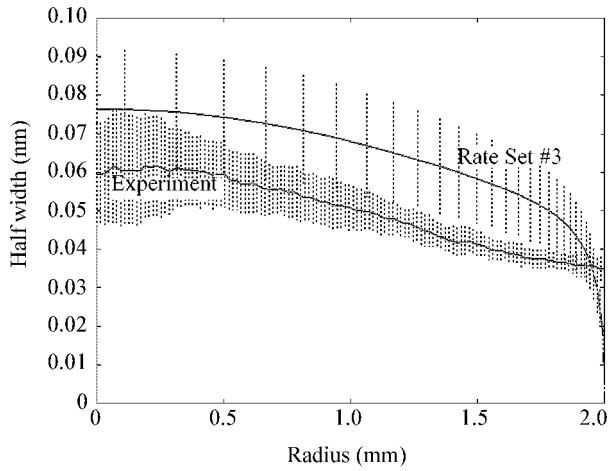

Fig. 8 Comparison of experimental and numerical radial distributions of H_α line widths (including uncertainty) in a 50-amp hydrogen arc at 1.34×10^4 Pa using chemical kinetic rate set #3 in the CAPS code.

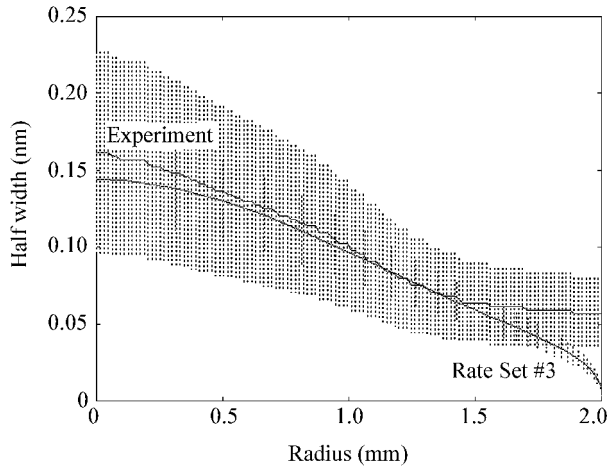

Fig. 9 Comparison of experimental and numerical radial distributions of H_α line widths (including uncertainty) in a 50-amp hydrogen arc at 4.14×10^4 Pa using chemical kinetic rate set #3 in the CAPS code.

The cascade arc emission line data are potentially degraded by three sources: self-absorption of the H_α line, high-frequency noise, and low-intensity signal.

Using the methods given by Boulos,[34] self-absoption has been shown to be negligible for both pressures. A detailed discussion of this analysis is given in Ref. 8.

The high-frequency noise is filtered during Abel inversion, and the associated error was calculated to be significant only for very small radii.[8] The low-intensity signal results in small signal-to-background-noiseratios across the entire arc. The maximum signal-to-noise ratios occur near the center of the arc and have values less than 2.4 for both pressures. As the edge of the arc is approached, the signal decreases substantially resulting in increasing uncertainty. Therefore, the simulated H_α emission line widths calculated from the CAPS code simulations with rate set #3 are believed to adequately predict the experimentally measured widths for the hydrogen arc at both pressures.

IX. Conclusions

Nonequilibrium plasma conditions of 50 A hydrogen arcs at 1.34×10^4 and 4.14×10^4 Pa have been measured and compared with computer simulations using the UTSI CAPS code. The simulations were run using an equilibrium model and three different sets of kinetic rates. The peak H_α line widths were consistently overpredicted by the equilibrium simulations. The simulated nonequilibrium plasma conditions using a finite-rate kinetic model were found to be extremely sensitive to the kinetic rates. The simulated nonequilibrium H_α line widths were less than the experimental values by as much as a factor of three and greater than the experimental values by as much as a factor of two, depending on the arc pressure and the kinetic rates used. The experimentally determined axial electric fields were bounded by the nonequilibrium computer simulation results using different sets of chemical kinetic rates. The axial electric field predicted using the CAPS code was also extremely sensitive to the finite-rate chemical kinetics utilized.

CAPS code simulations using the rate set #3 finite-rate chemical kinetics model match the measured electric fields and the radial distributions of H_α line widths within experimental uncertainty. The rate set #3 chemical kinetic rate set (taken from the University of Illinois arcjet simulations[1]), therefore, is believed to be the best finite-rate chemical kinetics set available for the simulation of hydrogen arc plasmas.

Chemical reaction set #3 is identical to chemical reaction set #2. However, the reaction rate for the dissociation of molecular hydrogen by electrons is substantially lower for rate set #3 than it is for rate set #2 (Ref. 24). All of the other chemical reactions have identical chemical kinetic rates. Yet, the rate set #3 simulations predict experimentally determined axial electric fields and electron number density distributions substantially better than the rate set #2 simulations. Therefore, the chemical kinetic rate set #3 results in more molecular hydrogen predicted across the radius of the arc. This implies that a higher fraction of molecular hydrogen in the simulation results is necessary to properly predict the hydrogen cascade arc plasma. To verify this implication, the radial distribution of molecular hydrogen density is needed. These values cannot be ascertained from the spectral data collected, but can be determined through Raman spectroscopy. The acquisition of this data and comparison with simulation results is left for future work.

Electron number density profiles for simulated ammonia and simulated hydrazine have been obtained for 50 A arcs at 1.34×10^4, 4.14×10^4, and 6.89×10^4 Pa. The measured electric field was found to vary directly with pressure and inversely with nitrogen content.

Acknowledgments

This work was supported by the U.S. Air Force Office of Scientific Research under contract #F49620-97-1-0223 and the National Science Foundation under NSF Grant #CTS-9512489. The authors would like to thank Nancy D. O'Brien for her invaluable assistance throughout the course of this research.

References

[1]Megli, T., Krier, H., and Burton, R., "A Plasmadynamics Model for Nonequilibrium Processes in N2/H2 Arcjets," AIAA Paper 95-1961, June 1995.

[2]Keefer, D., Burtner, D., Moeller, T., and Rhodes, R., "Multiplexed Laser Induced Fluorescence and Non-Equilibrium Processes in Arcjets," AIAA Paper 94-2656, June 1994.

[3]Miller, S., and Martinez-Sanchez, M., "Nonequilibrium Numerical Simulation of Radiation Cooled Arcjets," *Proceedings of the 23rd International Electric Propulsion Conference*, Vol. 3, Electric Rocket Propulsion Society, Ohio State Univ., Columbus, OH, 1993, pp. 2032–2050.

[4]Butler, G. W., Kashiwa, B. A., and King, D. Q., "Numerical Modeling of Arcjet Performance," AIAA Paper 90-1474, June 1990.

[5]Wiese, W. L., Paquette, D. R., and Solarski, J. E., "Profiles of Stark-Broadened Balmer Lines in a Hydrogen Plasma," *Physical Review*, Vol. 129, No. 3, 1963, pp. 1225–1232.

[6]Moeller, T., Keefer, D., and Rhodes, R., "Cascade Arc Studies of Nonequilibrium Hydrogen Plasmas," AIAA Paper 96-3294, July 1996.

[7]Rhodes, R., and Keefer, D., "Non-Equilibrium Modeling of Hydrogen Arcjet Thrusters," *Proceedings of the 23rd International Electric Propulsion Conference*, Vol. 3, Electric Rocket Propulsion Society, Ohio State Univ., Columbus, OH, 1993, pp. 2020–2031.

[8]Moeller, T. M., "Cascade Arc Studies of Nonequilibrium Hydrogen/Nitrogen Plasmas," Ph.D. Dissertation, Mechanical Engineering, Univ. of Tennessee Space Inst., Tullahoma, May 1998.

[9]Gosman, A. D., and Pun, W. M., "Calculation of Recirculation Flows," Dept. of Mechanical Engineering, Rept. HTS/74/12, Imperial College, London, Dec. 1974.

[10]Rhie, C. M., "A Pressure Based Navier–Stokes Solver," AIAA Paper 86-0207, Jan. 1986.

[11]Moeller, T. M., "Comparison of Experimental and Numerical Results for Radiation Cooled and Water Cooled Hydrogen Arcjets," *Proceedings of the 23rd International Electric Propulsion Conference*, Vol. 3, Electric Rocket Propulsion Society, The Ohio State Univ., Columbus, OH, 1993, pp. 1979–1988.

[12]Jeng, S.-M., and Keefer, D., "Theoretical Evaluation of Laser-Sustained Plasma Thruster Performance," *Journal of Propulsion and Power*, Vol. 5, No. 5, 1989, pp. 577–581.

[13]Rhodes, R. P., and Keefer, D., "Numerical Modeling of a Radio Frequency Plasma in Argon," *AIAA Journal*, Vol. 27, No. 12, 1989, pp. 1779–1784.

[14]Rhodes, R., and Keefer, D., "Comparison of Model Calculations with Experimental Data from Hydrogen Arcjets," *AIDAA/AIAA/DGLR/JSASS 22nd International Electric Propulsion Conference*, Paper 91-111, Oct. 1991.

[15]Park, C., *Non-Equilibrium Hypersonic Aerothermodynamics*, Wiley, New York, 1990.

[16]Griem, H., *Plasma Spectroscopy*, McGraw–Hill, New York, 1964.

[17]Mikatarian, R. R., Kau, C. J., and Pergament, H. S., "A Fast Computer Program for Nonequilibrium Rocket Plume Predictions," AeroChem, TP-282, Aug. 1972.

[18]Kuo, K. K., *Principles of Combustion*, Wiley, New York, 1986, pp. 109–155.

[19]Cho, K. Y., "Non-Equilibrium Thermodynamic Models and Applications to Hydrogen Plasmas," Ph.D. Dissertation, Mechanical Engineering, Georgia Inst. of Technology, March 1988.

[20]DeVoto, R. S., "The Transport Properties of a Partially Ionized Monatomic Gas," Ph.D. Dissertation, Stanford Univ., CA, 1965.

[21]Chapman, S., and Cowling, T. G., *Mathematical Theory of Non-Uniform Gases*, 3rd ed., Cambridge Univ. Press, New York, 1970.

[22]Hirschfelder, J. O., Curtiss, C. F., and Bird, R. B., *Molecular Theory of Gases and Liquids*, Wiley, New York, 1964.

[23]Siegal, R., and Howell, J. R., *Thermal Radiation Heat Transfer*, 3rd ed., Hemisphere, Washington, DC, 1992, pp. 751–754.

[24]Janev, R. K., Langer, W. D., Evans, K. Jr., and Post, D. E. Jr., *Elementary Processes in Hydrogen Helium Plasmas*, Springer-Verlag, New York, 1987, pp. 34–55.

[25]Gonzalez, R., and Wintz, P., *Digital Image Processing*, Addison Wesley Longman, Reading, MA, 1977, pp. 199–209.

[26]Oza, D. H., Greene, R. L., and Kelleher, D. E., "Collisional Broadening of the Balmer-α Transition of H and He+ in Plasmas," *Physical Review A*, Vol. 37, No. 2, 1988, pp. 531–536.

[27]Oza, D. H., Greene, R. L., and Kelleher, D. E., "Dependence of the Half Width of Plasma-Broadened Hydrogen Lines on Reduced Mass, Temperature, and Density," *Physical Review A*, Vol. 38, No. 5, 1988, pp. 2544–2551.

[28]Kelleher, D. E., Wiese, W. L., Helbig, V., Greene, R. L., and Oza, D. H., "Advances in Plasma Broadening of Atomic Hydrogen," *Physica Scripta*, Vol. T47, 1993, pp. 75–79.

[29]Griem, H. R., "Stark Broadening of the Hydrogen Balmer-α Line in Low and High Density Plasmas," *Contributions to Plasma Physics*, Vol. 40, No. 1-2, 2000, pp. 46–56.

[30]Moeller, T., Keefer, D., and Rhodes, R., " Studies of Nonequilibrium Hydrogen/Nitrogen Plasmas Using a Cascade Arc," *AIP Conference Proceedings 387*, American Inst. of Physics, Woodbury, NY, 1997, p. 317.

[31]Moeller, T., Keefer, D., and Rhodes, R., "Nonequilibrium Hydrogen/Nitrogen Plasmas Studies Using a Cascade Arc," *Proceedings of the 25th International Electric Propulsion Conference*, Electric Rocket Propulsion Society, Columbus, Ohio, 1997.

[32]Smith, L. M., Keefer, D., and Sudharsanan, S. I., "Abel Inversion Using Transform Techniques," *Journal of Quantitative Spectroscopy and Radiation Transfer*, Vol. 39, No. 5, 1988, pp. 367–373.

[33]Smith, L. M., "Nonstationary Noise Effects in the Abel Inversion," *IEEE Transactions on Information Theory*, Vol. 34, No. 1, 1988, pp. 158–161.

[34]Boulos, M. I., Fauchais, P., and Pfender, E., *Thermal Plasmas Fundamentals and Applications*, Vol. 1, Plenum, New York, 1994, pp. 325–344.